Available online at www.sciencedirect.com

ScienceDirect

Procedia Structural Integrity 61 (2024) 26–33

Structural Integrity Procedia

www.elsevier.com/locate/procedia

3rd International Workshop on Plasticity, Damage and Fracture of Engineering Materials (IWPDF 2023)

Experimental and Numerical Investigation of Ductile Damage and Fracture Under Biaxial Reverse Loading Conditions

Zhichao Wei[a,*], Steffen Gerke[a], Michael Brünig[a]

[a]*Institut für Mechanik und Statik, Universität der Bundeswehr München, Werner-Heisenberg-Weg 39, D-85577 Neubiberg, Germany*

Abstract

This paper deals with the experimental and numerical analysis of plasticity, damage, and fracture of the aluminum alloy EN AW 6082-T6. The HC-specimen is designed to study the material response under biaxially monotonic and reverse loading conditions. Moreover, a modified anisotropic stress-state-dependent plastic-damage continuum model incorporating combined hardening and softening rules is proposed to predict the plastic, damage, and fracture behavior. Non-proportional loaded shear monotonic and cyclic tests superimposed by tensile preloads 6 kN and 9 kN are performed to capture different stress states and to validate the proposed material model. Moreover, the digital image correlation (DIC) technique monitors and analyzes the deformations and strain fields in critical regions of the specimen, and scanning electron microscopy (SEM) is additionally used to verify damage and fracture mechanisms.

Keywords: Ductile damage and fracture; Non-proportional biaxial experiments; Reverse loading; Numerical modeling

1. Introduction

Damage is an irreversible process during loading conditions. The accumulation of damage significantly degrades the material's elastic behavior and, eventually, causes it to fracture. Therefore, accurately capturing the evolution of damage through experiments and numerical simulations has been an active area of research in recent decades. Although many studies on the behavior of metal sheets are based on uniaxial experiments (Kanvinde and Deierlein, 2007; Voyiadjis et al., 2012; Roth et al., 2018; Algarni et al., 2019; Shen et al., 2024), the engineering structures are frequently subjected to non-proportional multi-axial cyclic loading in various manufacturing processes and applications. Moreover, biaxially loaded cruciform specimens are used to study the plastic, damage, and fracture behavior under proportional or non-proportional loading conditions (Kulawinski et al., 2011; Papasidero et al., 2015; Cortese et al., 2016; Iftikhar and Khan, 2021; Raj et al., 2022; Hou et al., 2022). Compared to proportional loading, non-proportional

* Corresponding author. Tel.: +49-89-60043413 ; fax: +49-89-60043413.
E-mail address: zhichao.wei@unibw.de

2452-3216
10.1016/j.prostr.2024.06.005

loading histories significantly influence the material behavior by altering the loading directions. For instance, pre-tensile loading leads to an increase in the brittleness of the ductile aluminum alloy, whereas pre-compressive loading results in an increase in the ductility of the material (Kong et al., 2023; Wei et al., 2023). However, it is essential to note that these previous studies have mainly focused on monotonic or non-proportional loading histories. Recently, it has been observed that the damage and fracture behavior is remarkably influenced by different reverse loading conditions (Kanvinde and Deierlein, 2007; Voyiadjis et al., 2013; Marcadet and Mohr, 2015; Daroju et al., 2022; Wei et al., 2022). Micro-defects become more accessible to coalescence with neighboring ones, leading to larger and denser micro-defects and further significant material degradation after reverse loading. Therefore, a new series of biaxially loaded shear single-cyclic experiments has been designed and conducted to fill this gap and gain a deeper understanding of the material response. Wei et al. (2023) conducted experiments with preloads up to 5 kN, limiting the stress triaxiality to 0.33. To extend the generation of stress triaxiality, experiments with tensile preloads of 6 kN and 9 kN are designed in the present work. These newly designed loading paths fill the gap in generating high stress triaxialities and enable the capture of damage and fracture behavior under higher stress triaxialities. Furthermore, the digital image correlation (DIC) technique and scanning electron microscopy (SEM) are employed to provide a more accurate characterization of the material behavior during and after the experiments.

Concerning the numerical modeling aspects, an anisotropic plastic-damage continuum model (Wei et al., 2022, 2023) is proposed in the present work. For plasticity, the Drucker-Prager yield condition incorporates the combined hardening rule and the change in the hardening ratio after reverse loading (Wei et al., 2023). In the damage modeling, the damage condition and damage strain rate tensor depend on the stress states, enabling accurate predictions of tensile-dominated, shear-dominated, and mixed damage mechanisms. Furthermore, a combined softening rule is introduced to characterize the changes in the damage surface under cyclic loadings. Additionally, the proposed continuum model has been successfully implemented as a user-defined subroutine in ANSYS, and the details of the numerical integration algorithm can be found in Wei et al. (2024). In this paper, the experimental material and loading path are described in Section 2. Moreover, the constitutive model is briefly discussed in Section 3, and the corresponding experimental and numerical results are presented in Section 4.

2. Experiments

2.1. Material and specimen geometry

The investigated material in this work is the high-strength aluminum-magnesium-silicon (AlMgSi) alloy EN-AW 6082-T6, with suitable welding and machining properties. Young's modulus is $E = 67.5$ GPa and Poisson's ratio $\nu = 0.29$. As shown in Fig. 1, the HC-specimen has four symmetric notches in the center of the specimen, and the details of the notched region are shown in Figs. 1(b)–(c). The length of box axes is 240 mm, and the widths of axes 1 and 2 are 20 mm and 32 mm, respectively. Moreover, the tension or compression reaction force F_2 is generated by applying machine displacements $u^M_{2,1}$ and $u^M_{2,2}$ only along the horizontal axis, see Fig. 1(d). On the other hand, the shear force F_1 is obtained by imposing machine displacements $u^M_{1,1}$ and $u^M_{1,2}$ along the vertical axis. The digital image correlation (DIC) technique is utilized to record and analyze deformations, where F_i and u_i are obtained. It is important to note that the displacements u_i measured by DIC differ from the machine displacement $u^M_{1,1}$. To compare the experimental and numerical results concerning force-displacement curves, the mean forces and relative displacements are calculated as

$$F_i = \frac{F_{i,1} + F_{i,2}}{2}, \quad \text{and} \quad \Delta u_{ref} = u_{i.1} + u_{i.2}\,, \tag{1}$$

respectively, see Fig. 1.

2.2. Loading paths

As shown in Fig. 2, the loading process is divided into two separate steps: (a) the displacement u^M_2 is imposed in axis 2 and $F_1 = 0$ until the targeted force $F_2 = 6$ kN or 9 kN is achieved; (b) the monotonic (Fig. 2(a)) or cyclic (Fig. 2(b)) u^M_1 is applied on axis 1 superimposed by the targeted force (6 kN or 9 kN) in axis 2. It must be emphasized

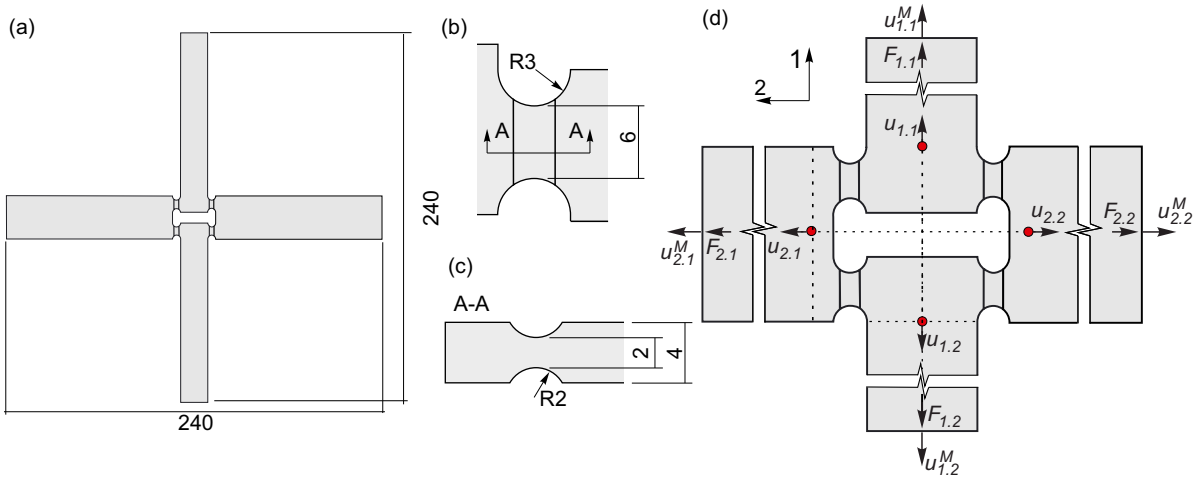

Fig. 1: HC-specimen geometry; all units in [mm].

that using force-control in axis 2 leads to non-negligible machine displacement u_2^M, as depicted in Fig. 2, u_2^M keeps increasing during the loading process. A biaxial testing routine is summarized as follows:

- The machine displacement $u_{2.1}^M$ in cylinder 2.1 is proportionally imposed in the positive direction with a machine speed of 0.004 mm/s until the reaction force $F_{2.1}$ reaches 6 kN or 9 kN. No machine displacement, i.e., $u_{1.1}^M = 0$, is applied to cylinder 1.1.
- The machine displacements $u_{1.2}^M = u_{1.1}^M$ and $u_{2.2}^M = u_{2.1}^M$ are applied to cylinders 1.2 and 2.2, respectively, as shown in Fig. 1(d).
- Subsequently, monotonic or cyclic machine displacement $u_{1.1}^M$ is proportionally applied to cylinder 1.1 until specimen failure. Additionally, cylinder 2.1 is force-driven with a respective force of 6 kN or 9 kN.
- The machine displacements $u_{1.2}^M = u_{1.1}^M$ and $u_{2.2}^M = u_{2.1}^M$ are applied to cylinders 1.2 and 2.2, respectively.

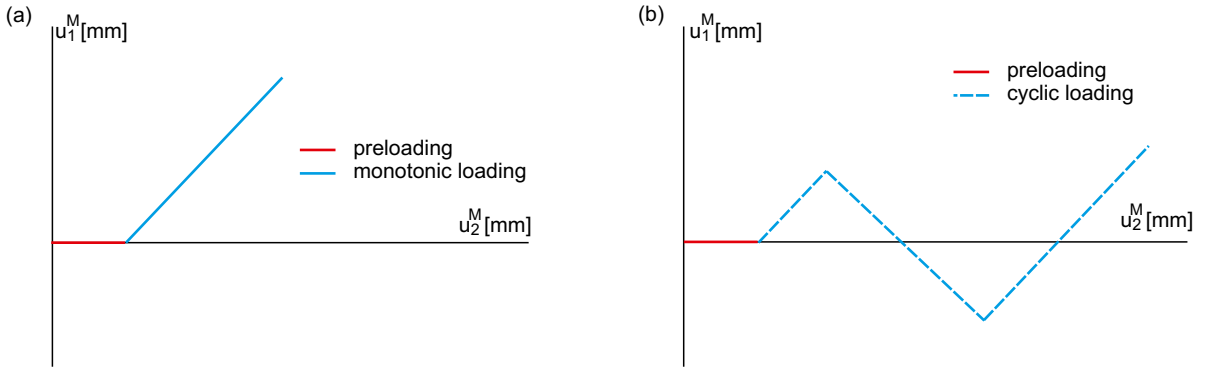

Fig. 2: Schematic sketch for the loading paths: (a) monotonic loading and (b) cyclic loading.

In this paper, monotonic loading and cyclic loading are abbreviated as mon and cyc, respectively. Thus, mon-T6 and cyc-T6 denote the monotonic and cyclic shear loading applied on axis 1 superimposed by $F_2 = 6$ kN in axis 2, respectively. Similar symbols mon-T9 and cyc-T9 are used in the same way.

3. Theoretical framework

The proposed material model is briefly summarized in this section. Please refer to (Wei et al., 2022, 2023, 2024) for further details. The plastic material parameters, describing the isotropic and kinematic hardening rules, are identified using the uniaxial monotonic and cyclic tension-compression tests. The original experimental data and fitting strategy are described in Wei et al. (2022). Furthermore, the isotropic and kinematic softening parameters are inversely calibrated by analyzing the micro-simulations with an initial micro-void.

3.1. Plasticity

As highlighted by Wei et al. (2022) for the investigated aluminum alloy EN AW 6082-T6, the compressive yield stress differs from the tensile one by comparing the monotonic uniaxial compression and tension tests. Furthermore, the Bauschinger effect is notably observed in both uniaxial tension-compression and one-axial shear cyclic tests. Thus, the Drucker-Prager yield criterion incorporated with the combined hardening law

$$f^{\mathrm{pl}} = \sqrt{\frac{1}{2}\mathrm{dev}(\bar{\mathbf{T}} - \bar{\boldsymbol{\alpha}})\cdot\mathrm{dev}(\bar{\mathbf{T}} - \bar{\boldsymbol{\alpha}})} - \bar{c}(1 - \frac{a}{\bar{c}}\,\mathrm{tr}(\bar{\mathbf{T}} - \bar{\boldsymbol{\alpha}})) = 0 \tag{2}$$

is used to model the plastic deformations in the undamaged configurations, where $\bar{\mathbf{T}}$ denotes the effective Kirchhoff stress tensor, $\bar{\boldsymbol{\alpha}}$ represents the effective back stress tensor, $\bar{c}$ characterizes the current effective yield stress, and $a/\bar{c} = 32\,\mathrm{TPa}^{-1}$ is the constant hydrostatic coefficient, which can be determined by analyzing the uniaxial monotonic tensile and compressive experimental data (Wei et al., 2022).

The double Voce strain-hardening law

$$\bar{c} = c_0 + Q_1(1 - e^{-p_1\gamma}) + Q_2\xi(1 - e^{-p_2\gamma}) \tag{3}$$

describes the change in the shape of the current yield surface, where c_0 denotes the initial yield stress, and $Q_1 = 74.93\,\mathrm{MPa}$, $Q_2 = 21.32\,\mathrm{MPa}$, $p_1 = 8.96$ and $p_2 = 676.01$ are material constants. Additionally, ξ characterizes the different hardening behavior at the onset of plasticity under a wide range of strain states, see Wei et al. (2022, 2023).

Moreover, the modified non-linear Chaboche kinematic hardening law (Chaboche and Rousselier, 1983; Voyiadjis et al., 2013; Wei et al., 2022) is given by

$$\dot{\bar{\boldsymbol{\alpha}}}_1 = b_1\chi\dot{\bar{\mathbf{H}}}^{\mathrm{pl}} - b_2\chi\dot{\gamma}\bar{\boldsymbol{\alpha}}_1\,, \quad \dot{\bar{\boldsymbol{\alpha}}}_2 = b_3\dot{\bar{\mathbf{H}}}^{\mathrm{pl}} - b_4\dot{\gamma}\bar{\boldsymbol{\alpha}}_2\,, \quad \text{and} \quad \dot{\bar{\boldsymbol{\alpha}}}_3 = b_5\dot{\bar{\mathbf{H}}}^{\mathrm{pl}} - (1 - \cos^2\theta)b_6\dot{\gamma}\bar{\boldsymbol{\alpha}}_3\,, \tag{4}$$

and it is introduced to predict the transformation of the current yield surface under revere loading condition, where $b_1 = 61250\,\mathrm{MPa}$, $b_2 = 1750$, $b_3 = 895\,\mathrm{MPa}$, $b_4 = 15$, $b_5 = 115\,\mathrm{MPa}$, and $b_6 = 7.5$ are material constants, $\dot{\bar{\mathbf{H}}}^{\mathrm{pl}}$ denotes the rate of effective plastic strain tensor, $\chi = 0.8e^{-300\gamma} + 0.2$ represents an exponential Decay function for the cumulative equivalent plastic strain γ, and θ is angle parameter, see (Wei et al., 2022) for further details.

3.2. Damage

The stress-state-dependent damage condition incorporating the combined softening rule

$$f^{\mathrm{da}} = \hat{\alpha}\,\mathrm{tr}(\mathbf{T} - \boldsymbol{\alpha}) + \hat{\beta}\sqrt{\frac{1}{2}\mathrm{dev}(\mathbf{T} - \boldsymbol{\alpha})\cdot\mathrm{dev}(\mathbf{T} - \boldsymbol{\alpha})} - \tilde{\sigma} = 0 \tag{5}$$

is introduced, where $\mathbf{T}$ and $\boldsymbol{\alpha}$ are the Kirchhoff stress tensor and the damage back stress tensor, respectively. $\tilde{\sigma}$ represents the current equivalent softening stress, as well as $\hat{\alpha}$ and $\hat{\beta}$ are the stress-state-dependent coefficients.

Furthermore, the damage strain evolution equation in damaged configurations is given by

$$\dot{\mathbf{H}}^{\mathrm{da}} = \dot{\mu}(\tilde{\alpha}\frac{1}{\sqrt{3}}\mathbf{1} + \tilde{\beta}\tilde{\mathbf{N}})\,, \tag{6}$$

where $\dot{\mu}$ denotes the rate of the equivalent damage strain, $\tilde{\alpha}$ and $\tilde{\beta}$ are damage parameters, and $\tilde{\mathbf{N}}$ is the transformed reduced stress tensor.

The exponential isotropic softening law is defined as

$$\tilde{\sigma} = \tilde{\sigma}_0 - C_1 e^{-C_2 \mu} \tag{7}$$

with the initial equivalent damage stress $\tilde{\sigma}_0 = 270\,\text{MPa}$, and the damage material constants $C_1 = 0.004207\,\text{MPa}$ and $C_2 = 92.97$. Moreover, the non-linear kinematic softening law is proposed as

$$\dot{\boldsymbol{\alpha}} = d_1 \dot{\mathbf{H}}^{\text{da}} - d_2 \dot{\mu} \boldsymbol{\alpha}\,, \tag{8}$$

where $d_1 = -0.51\,\text{MPa}$ is damage modulus and $d_2 = -84$ is damage material constant.

4. Experimental and numerical results

The numerical simulations are performed in ANSYS using implemented user-defined subroutines. The numerical simulations utilize one-fourth of the geometry, with a fine mesh ($0.25\,\text{mm} \times 0.125\,\text{mm} \times 0.1\,\text{mm}$) in the notch region. Displacement control is initially employed in the preloading axis (axis 2) until the designed preloads (6 kN or 9 kN) are reached. Subsequently, the force control approach is used on axis 2, while the displacement control method is utilized on axis 1, similar to the experimental designs, see Section. 2.2. This section will discuss the different aspects of the experimental and numerical results involving force–displacement curves, strain fields, stress states, and SEM and fracture images.

4.1. Force-displacement curves

The experimental and numerical force-displacement curves for the tests mon-T6, cyc-T6, mon-T9, and cyc-T9 are shown in Fig. 3, and the numerical results agree well with the experimental ones in both axes. It can be observed that the proposed material model can capture the initial and reversal elastic-plastic transits force-displacement curves. The experimental fracture forces $F_1^{\text{fr,exp}}$ are 4.27 kN and 3.64 kN under monotonic and cyclic loading superimposed by $F_2 = 6\,\text{kN}$, respectively. Moreover, the corresponding experimental fracture displacements in axis 1 $\Delta u_1^{\text{fr,exp}}$ are 1.06 mm and 0.51 mm, respectively, and the fracture forces in axis 2 $\Delta u_2^{\text{fr,exp}} = 0.28\,\text{mm}$ and 0.31 mm, respectively. Notably, fracture displacement Δu_i^{fr} is defined as the displacement from zero force to the final fracture after the second reverse loading of the cyclic loading path. In addition, experiment mon-T9 failed at the fracture displacements $\Delta u_1^{\text{fr,exp}} = 0.46\,\text{mm}$ and $\Delta u_2^{\text{fr,exp}} = 0.11\,\text{mm}$ with the fracture force $F_1^{\text{fr,exp}} = 2.19\,\text{kN}$. In the case of the test cyc-T9, the fracture occurred at the displacements $\Delta u_1^{\text{fr,exp}} = 0.20\,\text{mm}$ and $\Delta u_2^{\text{fr,exp}} = 0.08\,\text{mm}$, and the fracture force $F_1^{\text{fr,exp}}$ arrived at 2.14 kN. Obviously, the fracture displacements and forces decrease with an increasing preload in axis 1. More importantly, the fracture displacements and forces under monotonic loading differ from the ones undergoing cyclic loading conditions. These findings reveal that the preload and loading pattern (monotonic or cyclic) significantly influence the global force-displacement curve. Moreover, the investigated aluminum alloy becomes more brittle under cyclic loading conditions compared to the monotonic ones.

4.2. Strain fields and stress states

The first principal strains A_1 distributions for monotonic and cyclic loading are shown in Fig 4. The numerically predicted A_1 distributions agree well with the experimental ones obtained from the DIC. The maximum first principal strains A_1 for tests mon-T6 and cyc-T6 are 0.34 and 0.23, respectively. Moreover, the first principal strain is distributed as an X-shape and localized on the left-top and right-bottom of the notch surface in the cyc-T6 experiment, indicating the alteration of the strain direction under reverse loading conditions, as illustrated in Fig. 4(b). On the other hand, the maximum principal strains for mon-T9 and cyc-T9 experiments are nearly the same, but the shear band for the mon-T9 test is narrower and more inclined than that one for the cyc-T9 test, Figs. 4(c)-(d). Clearly, the different preloads and loading patterns significantly affect the distribution of strains and plastic behavior.

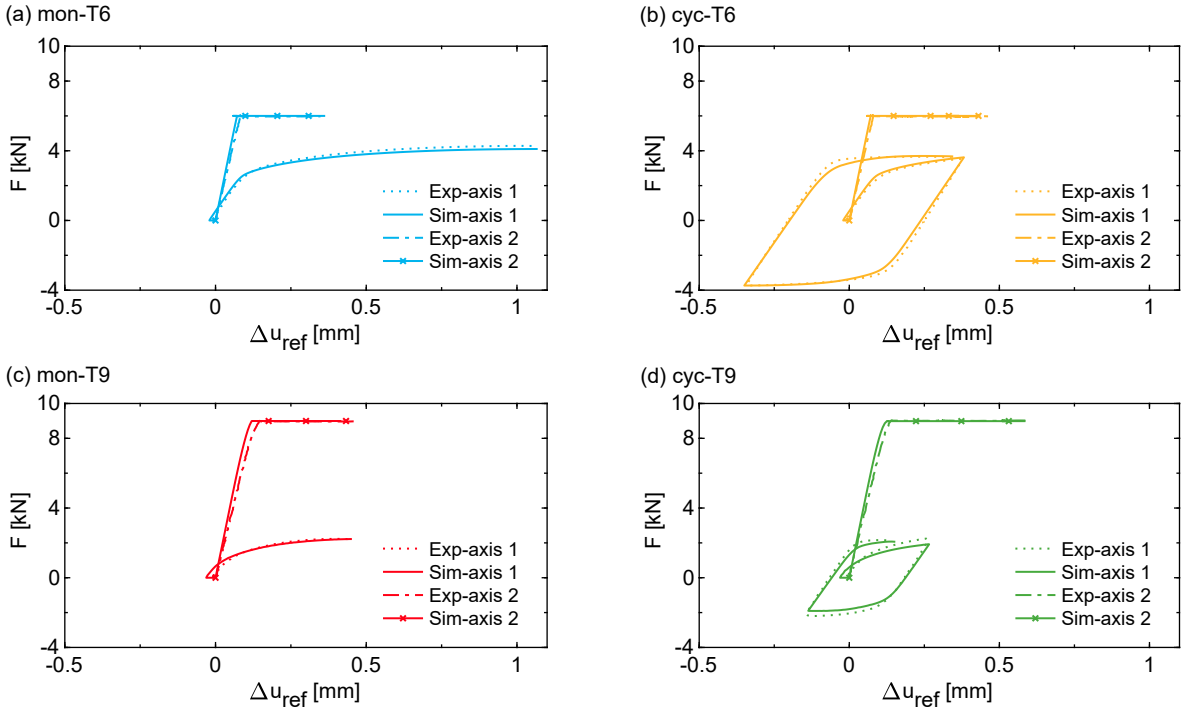

Fig. 3: Force-displacement curves for monotonic and cyclic tests.

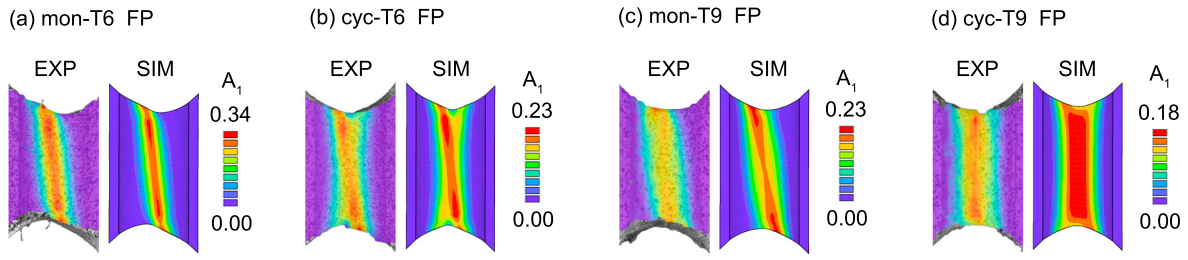

Fig. 4: Experimental and numerical distributions of the first principal strains A_1 on the notched surfaces (FP = fracture point).

The numerical prediction indicates inhomogeneous stress triaxialities η distributed across the notched cross-sections because stress tends to localize in the center of the notched cross-section. Thus, the mean stress triaxiality $\bar{\eta}$ is utilized to characterize the stress state for the numerical analysis and is defined as

$$\bar{\eta} = \frac{1}{S}\int_0^S \eta ds \quad \text{with} \quad \eta = \frac{I_1}{3\sqrt{3J_2}}, \tag{9}$$

where S denotes the total area of the notched cross-section, and $I_1 = \mathrm{tr}(\mathbf{T})$ and $J_2 = \frac{1}{2}\mathrm{dev}\mathbf{T} \cdot \mathrm{dev}\mathbf{T}$ are the first and second deviatoric stress invariants, respectively. The mean stress triaxialities for mon-T6, cyc-T6, mon-T9, and cyc-T9 experiments at FPs are 0.39, 0.43, 0.58, and 0.59, respectively. Different stress states are successfully generated by superimposing different preloads, with higher stress triaxialities induced by larger preloads. However, monotonic and cyclic loading patterns show only a slight difference. On the other hand, stress triaxialities slightly alter during the cyclic loading processes. For instance, the stress triaxialities for cyc-T9 at reverse point (RP1), reverse point (RP2), and FP are 0.59, 0.54, and 0.59, respectively. The stress triaxialities at RP1, RP2, and FP are 0.36, 0.37, and 0.43 for the cyc-T6 experiment.

Furthermore, the numerically predicted first principal damage strains A_1^{da} on the notch surfaces and notched cross-sections are shown in Fig. 5. For experiments superimposed by 6 kN, the maximum damage strain occurs on the notch surface for the mon-T6 test, whereas the maximum damage strain is observed on the notched edge surface in the cyc-T6 experiment. Moreover, the maximum principal damage strains are both numerically predicted on the center of the notched cross-section for mon-T9 and cyc-T9 tests, with maximum values of $A_1^{da} = 2.00\%$ and $A_1^{da} = 3.50\%$, respectively. In conclusion, the different preloads and loading patterns significantly influence stress states, damage occurrences, and developments.

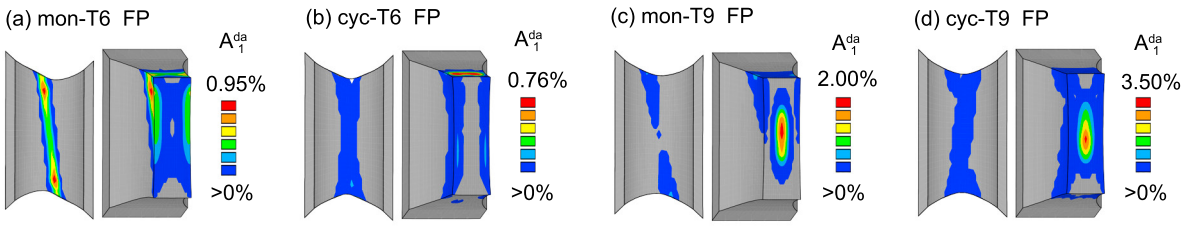

Fig. 5: Numerical distributions of the first principal damage strains A_1^{da} on the notched surfaces and notched cross-sections (FP = fracture point).

4.3. SEM and fracture pictures

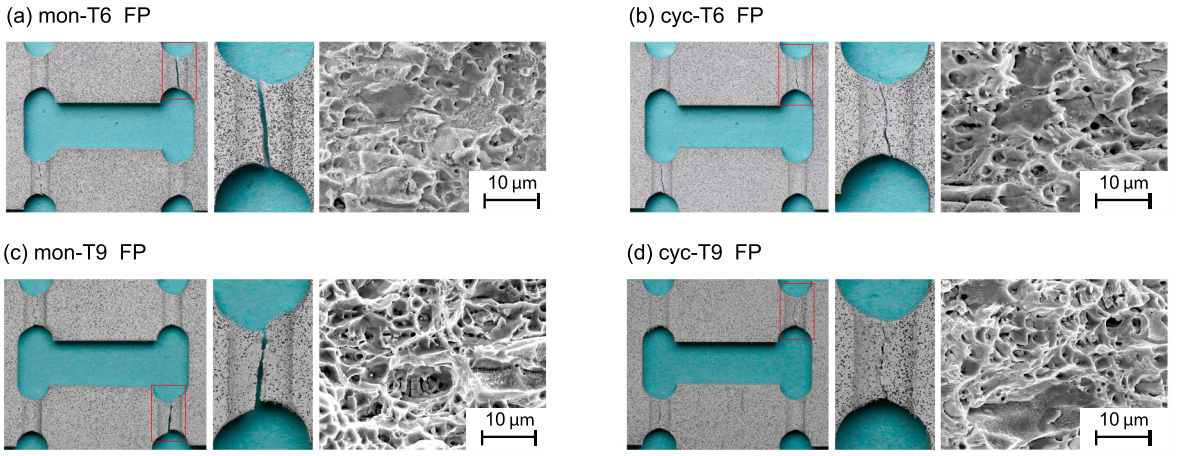

Fig. 6: Fracture pictures taken from the notch surfaces and SEM pictures taken from the fractured notched cross-sections (FP = fracture point).

As shown in Fig. 6, the specimens always break into two parts, and the fracture lines are distributed in the diagonal direction. It enables the analysis of the fractured notched cross-section using scanning electron microscopy (SEM), and all SEM images are taken from the critical positions. Moreover, the fracture lines in the tests with preload 9 kN exhibit a more irregular and jagged pattern than that one in the tests superimposed by 6 kN. In addition, micro-voids are visible on the fractured notched cross-sections. It highlights that the growth and coalescence of the micro-voids under high stress triaxialities results in further fracture behavior. Furthermore, larger and more coalesced micro-voids can be seen in the case of cyclic loading compared to monotonic loading. Comparing Figs. 6(c) and (a), it is evident that the depth of micro-voids increases with increased stress triaxiality. These facts indicate that the stress states and loading histories influence the material behavior at the microscopic level.

5. Conclusion

In the present work, non-proportional biaxial monotonic and cyclic experiments have been performed to study the plastic, damage, and fracture behavior. The experimental and numerical results indicate that preloads and loading patterns significantly affect the plastic, damage, and fracture behavior. The tests, superimposed by preloads of 6 kN and 9 kN, result in stress triaxialities of 0.4 and 0.6, respectively. Furthermore, SEM images reveal significant differences between the newly designed experiments and those reported in Wei et al. (2023). These findings suggest the significance of taking into account preloads and loading patterns when comprehending material responses under various loading conditions. The influence of varying preload magnitudes and preload patterns should be considered for discussion in future research. Moreover, experimental specimens can be examined metallographically with micrographs at different loading steps to monitor the microstructural change.

Acknowledgements

The project has been funded by the Deutsche Forschungsgemeinschaft (DFG, German Research Foundation) – project number 322157331, this financial support is gratefully acknowledged.

References

Algarni, M., Bai, Y., Zwawi, M., Ghazali, S., 2019. Damage evolution due to extremely low-cycle fatigue for Inconel 718 alloy. Metals 9, 1109.

Brünig, M., Gerke, S., Hagenbrock, V., 2013. Micro-mechanical studies on the effect of the stress triaxiality and the Lode parameter on ductile damage. Int. J. Plast. 50, 49–65.

Chaboche, J.L., Rousselier, G., 1983. On the Plastic and Viscoplastic Constitutive Equations—Part I: Rules Developed With Internal Variable Concept. J. Pressure Vessel Technol. 105, 153–158.

Cortese, L., Nalli, F., Rossi, M., 2016. A nonlinear model for ductile damage accumulation under multiaxial non-proportional loading conditions. Int. J. Plast. 85, 77–92.

Daroju, S., Kuwabara, T., Sharma, R., Fullwood, D.T., Miles, M.P., Knezevic, M., 2022. Experimental characterization and crystal plasticity modeling for predicting load reversals in AA6016-T4 and AA7021-T79. Int. J. Plast. 153, 103292.

Hou, Y., Lee, M.G., Lin, J., Min, J., 2022. Experimental characterization and modeling of complex anisotropic hardening in quenching and partitioning (Q&P) steel subject to biaxial non-proportional loadings. Int. J. Plast. 156, 103347.

Iftikhar, C.M.A., Khan, A.S., 2021. The evolution of yield loci with finite plastic deformation along proportional and non-proportional loading paths in an annealed extruded AZ31 magnesium alloy. Int. J. Plast. 143, 103007.

Kanvinde, A.M., Deierlein, G.G., 2007. Cyclic Void Growth Model to Assess Ductile Fracture Initiation in Structural Steels due to Ultra Low Cycle Fatigue. J. Eng. Mech. 133, 701–712.

Kong, X., Morgeneyer, T.F., Missoum-Benziane, D., Rousselier, G., 2023. A polycrystalline damage model applied to an anisotropic aluminum alloy 2198 under non-proportional load path changes. Int. J. Plast. 168, 103674.

Kulawinski, D., Nagel, K., Henkel, S., Hübner, P., Fischer, H., Kuna, M., Biermann, H., 2011. Characterization of stress–strain behavior of a cast TRIP steel under different biaxial planar load ratios. Eng. Fract. Mech. 78, 1684–1695.

Marcadet, S.J., Mohr, D., 2015. Effect of compression–tension loading reversal on the strain to fracture of dual phase steel sheets. Int. J. Plast. 72, 21–43.

Papasidero, J., Doquet, V., Mohr, D., 2015. Ductile fracture of aluminum 2024-T351 under proportional and non-proportional multi-axial loading: Bao–Wierzbicki results revisited. Int. J. Solids Struct. 69-70, 459–474.

Raj, A., Verma, R.K., Singh, P.K., Shamshoddin, S., Biswas, P., Narasimhan, K., 2022. Experimental and numerical investigation of differential hardening of cold rolled steel sheet under non-proportional loading using biaxial tensile test. Int. J. Plast. 154, 103297.

Roth, C.C., Morgeneyer, T.F., Cheng, Y., Helfen, L., Mohr, D., 2018. Ductile damage mechanism under shear-dominated loading: In-situ tomography experiments on dual phase steel and localization analysis. Int. J. Plast. 109, 169–192.

Shen, F., Sparrer, Y., Rao, J., Könemann, M., Münstermann, S., Lian, J., 2024. A forming limit framework accounting for various failure mechanisms: localization, ductile and cleavage fracture. Int. J. Plast. , 103921.

Voyiadjis, G.Z., Hoseini, S.H., Farrahi, G.H., 2012. Effects of stress invariants and reverse loading on ductile fracture initiation. Int. J. Solids Struct. 49, 1541–1556.

Voyiadjis, G.Z., Hoseini, S.H., Farrahi, G.H., 2013. A Plasticity Model for Metals With Dependency on All the Stress Invariants. J. Eng. Mater. Technol. 135.

Wei, Z., Gerke, S., Brünig, M., 2023. Damage and fracture behavior under non-proportional biaxial reverse loading in ductile metals: Experiments and material modeling. Int. J. Plast. 171, 103774.

Wei, Z., Gerke, S., Brünig, M., 2024. Numerical analysis of non-proportional biaxial reverse experiments with a two-surface anisotropic cyclic plasticity-damage approach. Comput. Methods Appl. Mech. Eng. 419, 116630.

Wei, Z., Zistl, M., Gerke, S., Brünig, M., 2022. Analysis of ductile damage and fracture under reverse loading. Int. J. Mech. Sci. , 107476.